J. Opt. A: Pure Appl. Opt. **10** (2008) 015007 (9pp) doi:10.1088/1464-4258/10/01/015007

Coupled surface plasmons on thin silver gratings

Z Chen, I R Hooper and J R Sambles

Thin Film Photonics Group, School of Physics, University of Exeter, Exeter EX4 4QL, UK

E-mail: J.R.Sambles@exeter.ac.uk

Received 12 September 2007, accepted for publication 13 November 2007
Published 12 December 2007
Online at stacks.iop.org/JOptA/10/015007

Abstract
A thin metal film with corrugations on both surfaces is shown to couple visible photons to both the long range surface plasmon polariton (LRSPP) and the short range surface plasmon polariton (SRSPP). It is found that the first harmonic component of the grating shape causes a significant band gap (an anti-crossing) where the LRSPP and the SRSPP should cross. Experimental data are compared with model calculations using a multilayer, multishape differential grating theory. In addition, to clarify the nature of the modes, the time averaged magnetic field distributions and instantaneous electric field profiles are explored, specifically at the anti-crossings of the first-order modes.

Keywords: surface plasmons, thin metal film, corrugations

1. Introduction

A surface plasmon polariton (SPP) is a fundamental electromagnetic excitation which may exist at the interface between a metal and a dielectric [1]. On a flat metal surface, an SPP mode cannot be directly excited by incident radiation because the dispersion curve of the SPP is outside the light cone (the in-plane momentum is greater than that available for a grazing photon in the adjacent dielectric). In order to optically excite the SPP mode, the in-plane momentum of the incident radiation must be suitably increased. This momentum enhancement may generally be achieved by using a coupling prism as in the Otto [2] or Kretschmann–Raether [3] geometry, or employing a surface relief grating [4–6]. In the case of grating coupling, the wavevector of the incident light is changed by the addition or subtraction of integer multiples of the grating wavevector via diffraction, making direct coupling between the SPP and radiation possible. For a sufficiently thick (optically opaque) metal film there is only one SPP mode, described as the single interface SPP (SISPP) [7]. However, for thinner metal layers (<100 nm) bounded by dielectrics with identical dielectric functions, the SISPPs on the two interfaces are degenerate and will interfere with one another to form two coupled SPPs, described as the long range SPP (LRSPP) and the short range SPP (SRSPP). Thus at the same in-plane momentum two coupled SPP modes of different frequencies will be formed which are distinguished by having different surface charge density distributions. The higher frequency LRSPP mode has an asymmetric charge distribution between the top and bottom surfaces with the electric field predominantly normal to the surface inside the metal. Conversely, the lower frequency SRSPP has a charge distribution which is symmetric between the top and bottom surfaces with the electric field essentially parallel to the surface. Over the last 30 years, resonant coupling of incident photons to LRSPP and SRSPP modes on both planar thin metal films [8–12] and corrugated thin metal films [13, 14] has been the subject of several studies. Excitement in this area of optical research was rekindled by the observation of substantially enhanced optical transmission through metallic films with a periodic array of subwavelength size holes by Ebbesen and co-workers [15–17]. They found unexpectedly high transmission peaks in their spectra, which may arise due to the excitation of surface plasmons on either side of the metal film [15, 16]. This suggests that coupled SPP modes on this type of structure may be important. Surprisingly there are rather few detailed experimental studies of simple corrugated thin metal films. Recently, Hooper *et al* [18] modelled coupled SPPs on thin metal slabs corrugated on both surfaces, where the corrugations on each side had the same pitch, 400 nm, a fundamental harmonic (k_g) amplitude of 10 nm, and a small first harmonic ($2k_g$) component of 5 nm (this was 90° out of phase with the k_g component). They reported a rather interesting evolution of the SISPP as the metal film was made

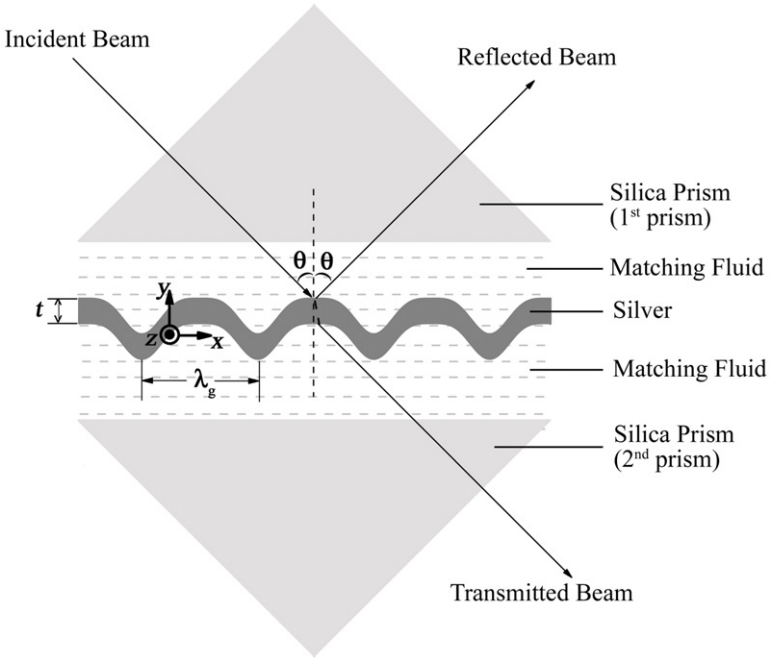

Figure 1. Schematic diagram illustrating the sample, coordinate system, and experimental geometry used in this work. Here λ_g is the grating pitch, t is the thickness of the silver layer, and θ is the polar angle.

thinner, with the band gap formed from the two standing wave SISPPs apparently moving away from the Brillouin zone centre and becoming an anti-crossing between the SRSPP and LRSPP modes. They noted that the LRSPP and SRSPP evolve directly from the high energy and low energy branches of the SISPP band gap modes.

In this study we investigate the SPP resonances of a free-standing thin silver film with identical corrugations on both sides.

2. Experiments and discussion

The geometry of the thin silver grating and associated coordinate system used in this study is shown in figure 1. In our experiments and modelling, we only consider the case for transverse magnetic (TM) polarized radiation incident at the fixed azimuth angle of $\varphi = 0°$ (grating grooves oriented perpendicular to the plane of incidence). The experimental sample is prepared by first depositing by thermal evaporation a 27 nm silver film onto a silica grating formed by optical lithography such that it contains a $2k_g$ component in addition to the fundamental k_g component with a pitch of $\lambda_g = 335$ nm. This structure is then converted into an optically symmetric system by the use of index matching fluid to couple two silica prisms symmetrically to the silver grating on its silica substrate. This forms an optically symmetric silver grating with respect to the silica medium. For clarity, we label the silica prism attached to the silica substrate the first prism, and the other attached to the silver the second prism.

The profile describing the thin silver grating is given by $[y_1(x) = a_0 \sin(k_g x) + a_1 \sin(2k_g x + \phi)]$ for the lower silver–silica interface and $[y_2(x) = a_0 \sin(k_g x) + a_1 \sin(2k_g x + \phi) + t]$ for the upper silver matching fluid interface. Here t is the mean thickness between the two surfaces, a_0 and a_1 are the amplitudes of the k_g and $2k_g$ components with $k_g = 2\pi/\lambda_g$ (λ_g is the grating pitch) the grating vector, which runs parallel to

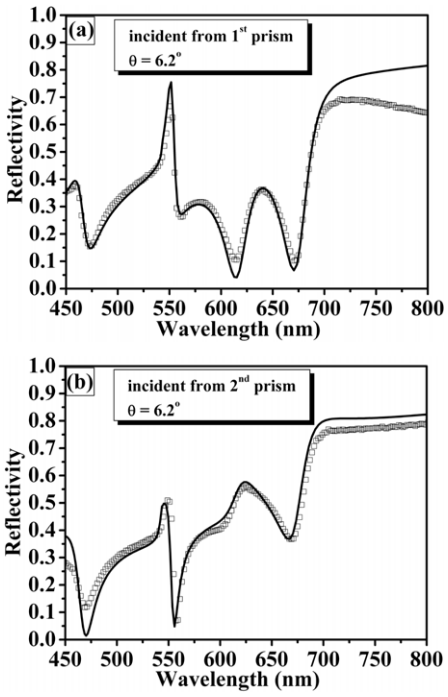

Figure 2. Typical wavelength-dependent absolute reflectivity data (open squares) together with the model fits (solid lines) when the light is incident at polar angle $\theta = 6.2°$ from (a) the first prism with a $+\pi/2$ phase shift between the first harmonic and the fundamental and (b) the second prism with $-\pi/2$ phase shift. The density of experimental data points has been reduced for clarity.

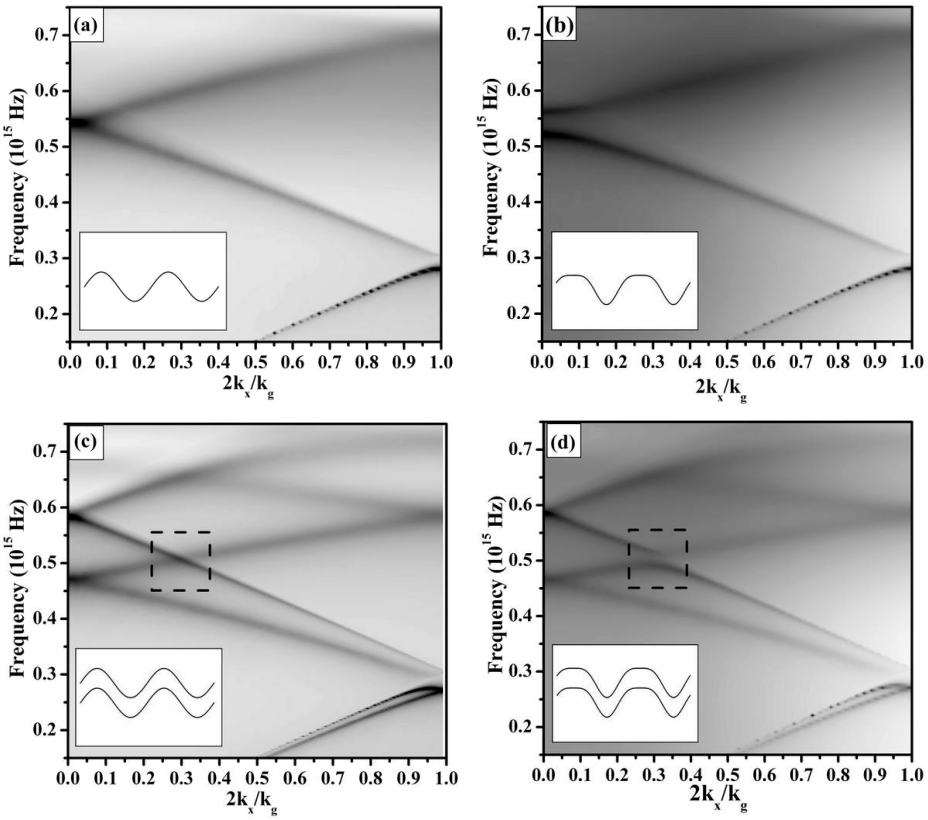

Figure 3. The model band structures for silver gratings having different profiles at an azimuth angle of $\varphi = 0°$. The profile describing the structures is given by (a) $[20\sin(k_g x)]$ nm; (b) $[20\sin(k_g x) + 5\sin(2k_g x + \pi/2)]$ nm; (c) $[20\sin(k_g x)]$ nm for the bottom surface and $[20\sin(k_g x) + 27]$ nm for the top surface; (d) $[20\sin(k_g x) + 5\sin(2k_g x + \pi/2)]$ nm for the bottom surface and $[20\sin(k_g x) + 5\sin(2k_g x + \pi/2) + 27]$ nm for the top surface. The inset graphs correspond to the gratings that have been used in the calculations. The dashed line box in the last two graphs indicates the crossing point that arises from scattering of the LRSPP by $+k_g$ and scattering of the SRSPP by $-k_g$.

the x axis. For an unblazed grating, as here, the phase shift ϕ between the $2k_g$ component and the k_g component must be $\pm\pi/2$. Then, dependent on from which side the radiation is incident, both the cases of $\phi = +\pi/2$ and $-\pi/2$ may be explored.

It is well known that in reflection the singly diffracted SPP modes of a single metal grating are shown as reflectivity minima in the zero-order beam, since the re-radiated light is in anti-phase with the specularly reflected light [1]. With light incident on one surface, because of the attenuation through the film, any re-radiated SPP light scattering from the other surface is much weaker than that re-radiated from the first surface, and so both the SRSPP and LRSPP are still seen as reflectivity minima. Hence, by measuring the reflectivity data as a function of wavelength (450 nm $\leqslant \lambda_0 \leqslant$ 800 nm) at various fixed polar angles and noting all the reflectivity minima, the dispersion diagram of the SPP modes associated with the structure for $\varphi = 0°$ is acquired.

Figure 2 illustrates the typical wavelength-dependent absolute reflectivity data together with the modelling results for light incident from the first prism and second prism respectively at a polar angle of $\theta = 6.2°$. The theoretical method employed here is based upon a conical version of the differential formalism originally developed by Chandezon *et al* [19], in which a nonorthogonal curvilinear coordinate transformation is used to allow for easy matching of the electromagnetic boundary conditions at the corrugated interfaces. This computational approach has been shown to agree well with experimental data in the past [20–22]. To model the silver across the visible spectrum both the real and imaginary parts of its permittivity are described by polynomials fitted to experimentally derived values [23]:

$$\varepsilon_r = -255.3185 + 198.63\omega - 60.794\omega^2 + 8.381\omega^3 - 0.430\,04\omega^4,$$

$$\varepsilon_i = 83.2575 - 132.79\omega + 90.474\omega^2 - 32.88\omega^3 + 6.6591\omega^4 - 0.708\,93\omega^5 + 0.030\,913\omega^6,$$

where $\omega = [2\pi c/\lambda]\times 10^{-15}$ s^{-1}. These polynomials inevitably pertain to somewhat different silver from that explored here in thin film form, but they are a good enough approximation to allow adequate modelling. Because of this, and for simplicity in fitting data to a model, the refractive index of the bounding silica is treated as non-dispersive with $n = 1.459$. In figure 2(a) (incident from the first prism), the best comparison between the model and the experimental data is achieved when the profiles of the two surfaces are set to $[20\sin(k_g x) + 5\sin(2k_g x + \pi/2) + 27]$ nm for the incident interface and $[20\sin(k_g x) + 5\sin(2k_g x + \pi/2)]$ nm for the transmitting interface. When the light is incident from the second prism

the phase shift ϕ between the $2k_g$ and k_g components changes sign from $+\pi/2$ to $-\pi/2$. Then using the profiles described as $[20\sin(k_g x) + 5\sin(2k_g x - \pi/2) + 27]$ nm for the incident interface and $[20\sin(k_g x) + 5\sin(2k_g x - \pi/2)]$ nm for the transmitting interface the theoretical modelling also agrees well with the experimental reflectivity data, as shown in figure 2(b).

For grating structures, due to the introduction of the periodicity, all of the modes in momentum space are 'reflected' at the Brillouin zone (BZ) boundary (Bragg scattering), resulting in crossing points between the different branches. Figure 3 shows the model band structures computed by inspection of the scattering matrices of the systems at an azimuth angle $\varphi = 0°$ over a range of frequencies and in-plane wavevectors (k_x) for silver gratings of different profiles. The profiles describing the structures in figures 3(a)–(d) are as follows: figure 3(a) $[20\sin(k_g x)]$ nm, figure 3(b) $[20\sin(k_g x) + 5\sin(2k_g x + \pi/2)]$ nm, figure 3(c) $[20\sin(k_g x)]$ nm for the bottom surface and $[20\sin(k_g x) + 27]$ nm for the top surface, and figure 3(d) $[20\sin(k_g x)+5\sin(2k_g x+\pi/2)]$ nm the for bottom surface and $[20\sin(k_g x) + 5\sin(2k_g x + \pi/2) + 27]$ nm for the top surface. In this work the focus of interest is the crossing points that arise through scattering of one wave by $-k_g$ and the other by $+k_g$. At these crossing points it is the $2k_g$ component of the profile which plays the primary role in producing any band gap [24]. Second-order scattering from the k_g component can also have a similar effect; however, this second-order process is very weak for the small amplitudes of the primary component used here and need not be considered in the present study. As shown in figures 3(a) and (b), the self-crossing point which arises from scattering by $\pm k_g$ only occurs at $k_x = 0$ (normal incidence). For a pure sinusoidal profile thick grating of the amplitude used here there is no significant splitting at this crossing point, as shown by the absence of a band gap in figure 3(a). However, if a $2k_g$ component is added to the profile, a band gap is observed at this crossing point, as shown in figure 3(b). The different energy SISPPs at the band edges are associated with the different positions of the surface charge density maxima (and hence optical field density distributions) with respect to the $2k_g$ component of the grating profile. The extrema of both the normal field component and the surface charge distribution for the higher energy SISPP mode occur at the troughs of the $2k_g$ component, whereas for the lower energy SISPP mode they are located at the peaks of the $2k_g$ component [24]. In the case of a thin film corrugated on both sides, the SISPP will split into two coupled LRSPP and SRSPP modes, and both of these might then be expected to be scattered by the $2k_g$ component, forming band gaps. As shown in figures 3(c) and (d), there are two crossing points at $k_x = 0$: one arises from the scattering of SRSPPs (at lower frequency) by $\pm k_g$, while the other (at higher frequency) arises from the scattering of LRSPPs. In addition to the self-crossing points, an additional third crossing point occurs in the BZ between $k_x = 0$ and $k_x = k_g/2$, as indicated by the dashed line box in figures 3(c) and (d). This arises from scattering of the LRSPP by $+k_g$ and scattering of the SRSPP by $-k_g$. In figure 3(c), because there is no $2k_g$ component there is no significant splitting at the crossing points. By contrast, as already indicated, when the $2k_g$ component is finite one expects band gaps to open up. Figure 3(d) clearly shows that at the third crossing point an anti-crossing occurs, while at the two self-crossing points at $k_x = 0$ no similar band gap appears, in stark contrast to figure 3(b). This is somewhat surprising. Later in this paper, we will discuss the splitting of the third crossing point and explain the reason for the lack of band gaps at the two self-crossing points (occurring at $k_x = 0$) even when there is a $2k_g$ component present in the structure.

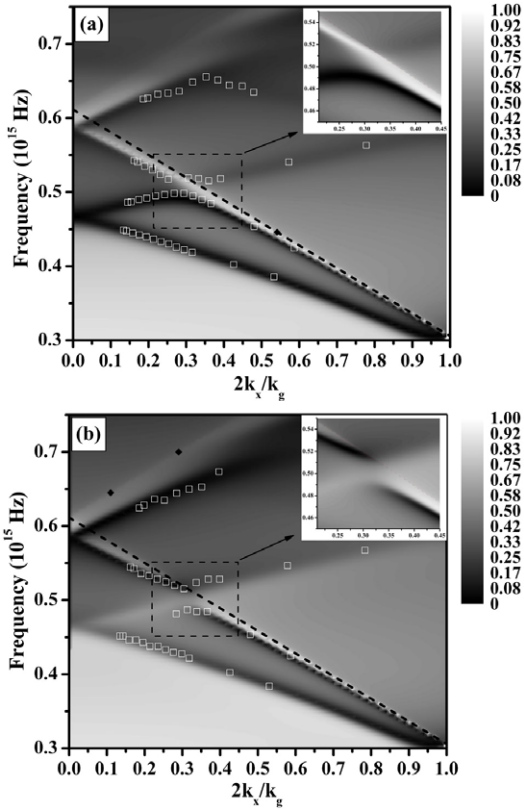

Figure 4. The model TM reflectivity as a function of frequency and in-plane wave vector with light incident from (a) the first prism and (b) the second prism. The open white squares are the mapped reflection dips that are taken from the experimental reflectivity spectra. The dashed straight line indicates the first-order diffracted light line. The dashed line box indicates the crossing point between the LRSPP and the SRSPP.

In addition to the wavelength-dependent absolute reflectivity data taken at polar angle $\theta = 6.2°$ as shown in figure 2, reflectivity data were also taken at 12 other polar angles ($\theta =$ 5.2°, 5.5°, 7.0°, 7.8°, 8.6°, 9.5°, 10.4°, 11.3°, 12.3°, 13.3°, 18.9°, and 25.0°) for both $\phi = +\pi/2$ and $-\pi/2$. Figure 4 shows the model reflectivity as a function of frequency and in-plane wave vector, with the experimental data (corresponding to the positions of the reflection minima) indicated as open white squares mapped onto this plot. The anti-crossing between the LRSPP and the SRSPP that occurs at $2k_x/k_g \approx 0.29$ is confirmed directly by the experimental data, as indicated by the dashed line boxes in figures 4(a) and (b). As expected, the LRSPP has approached the diffracted order light line, while the SRSPP has reduced in frequency with reduction in film thickness. These two effects are observed in figure 4 with

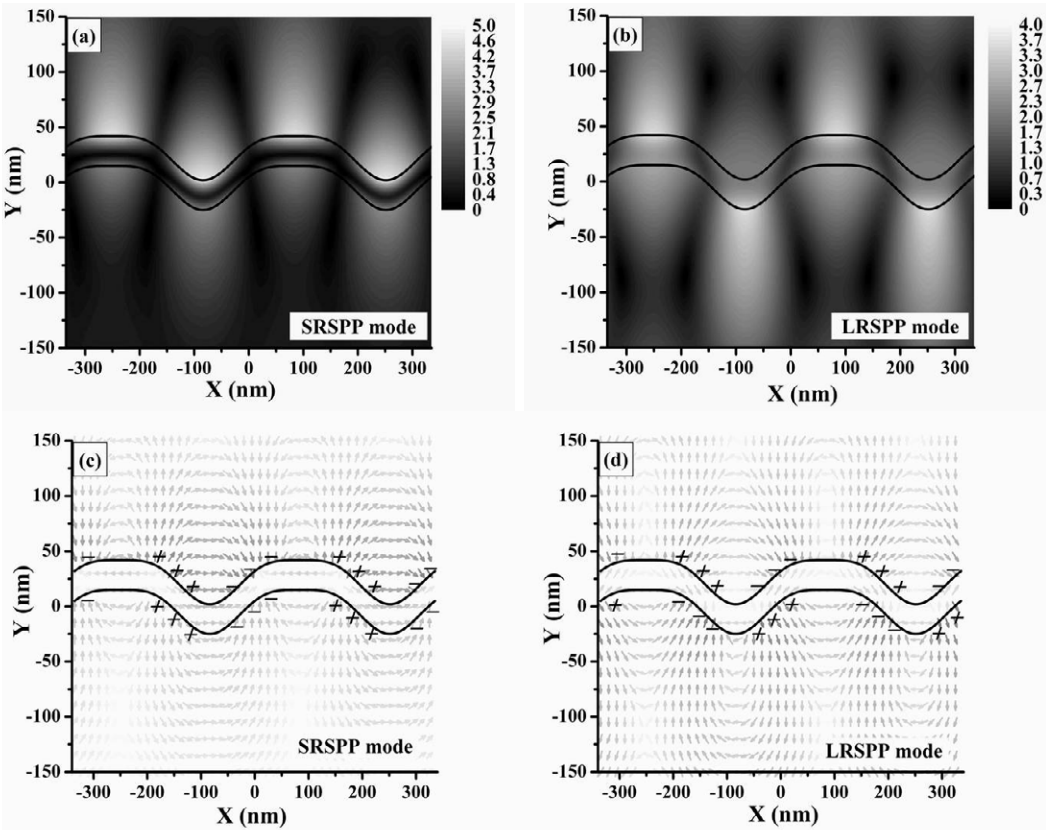

Figure 5. Time averaged H_z component of the fields of (a) the SRSPP and (b) the LRSPP modes that can be excited at normal incidence, together with the instantaneous E_{xy} vector fields for (c) the SRSPP and (d) the LRSPP modes on the same structure as described in figure 4(a) (incident from the first prism with $\phi = +\pi/2$). The continuous black lines represent the thin metal grating.

the first-order LRSPP modes (scattering from $+k_g$) being close to the diffracted light line (indicated as a dashed straight line) and the first-order SRSPP modes being further away from the diffracted light line.

We now turn our attention to the physics of the three crossing points mentioned previously. The lack of band gaps at the crossings of the forward and backward propagating LRSPPs and SRSPPs at normal incidence is a special case, and it will be discussed in detail later. The anti-crossing behaviour evident when the LRSPP and SRSPP cross at finite k_x on the other hand is readily understandable. Typically, when any two modes of appropriate symmetry cross each other anti-crossing behaviour is likely since the interaction strength between the two modes, caused by their field overlap, is rarely zero. Thus it is not surprising that an interaction, and hence a band gap, is evident in this case.

An explanation of the lack of band gaps at the crossings of the forward and backward propagating LRSPPs and SRSPPs at $k_x = 0$ is somewhat more complicated, however. In this case it is helpful to investigate the time averaged H_z component of the field distributions and the instantaneous E_{xy} vector fields for these two coupled SPP modes. In figure 5 we plot the H_z profiles together with the instantaneous E_{xy} vector fields of the SRSPP ($f = 0.467 \times 10^{15}$ Hz) and the LRSPP ($f = 0.579 \times 10^{15}$ Hz) modes excited at normal incidence ($\theta = 0°$) on the structure as described for figure 4(a) (incident from the first prism with $\phi = +\pi/2$). First note the different surface charge density distributions for the SRSPP and the LRSPP. As shown in figure 5(c), for the SRSPP, the spatial variation of the surface charge density distribution along the bottom surface is in phase with that on the top surface (symmetric distribution), while for the LRSPP in figure 5(d), the bottom surface has the opposite surface charge density to the top surface. Also note that, as shown in figures 5(a) and (b), the H_z component has a region of zero value inside the thin metal film for the SRSPP, while there is no such region for the LRSPP. By comparing figures 5(c) and (d), we can also see that the maximum surface charge density for both the SRSPP and the LRSPP occur on the sides of the grating grooves. This is because at normal incidence there will be no component of the electric field normal to the surface where the surface has zero gradient; hence only the modes with surface charge density maxima on the sides of the grating grooves may couple to the incident light. The key issue here is then the position of these surface charge density maxima relative to the $2k_g$ component of the grating. We know that for a single interface grating, the $2k_g$ component opens up a band gap where the modes cross each other, with the higher energy (ω^+) band edge having its surface charge density maxima at the troughs of the $2k_g$ component, and the lower energy (ω^-) band edge having its surface charge density maxima located at the peaks of the $2k_g$ component. Now we should consider the role that the $2k_g$ component plays in the thin metal grating structure at normal incidence. As mentioned above, at $k_x = 0$ there are two self-crossing points caused by two LRSPP modes

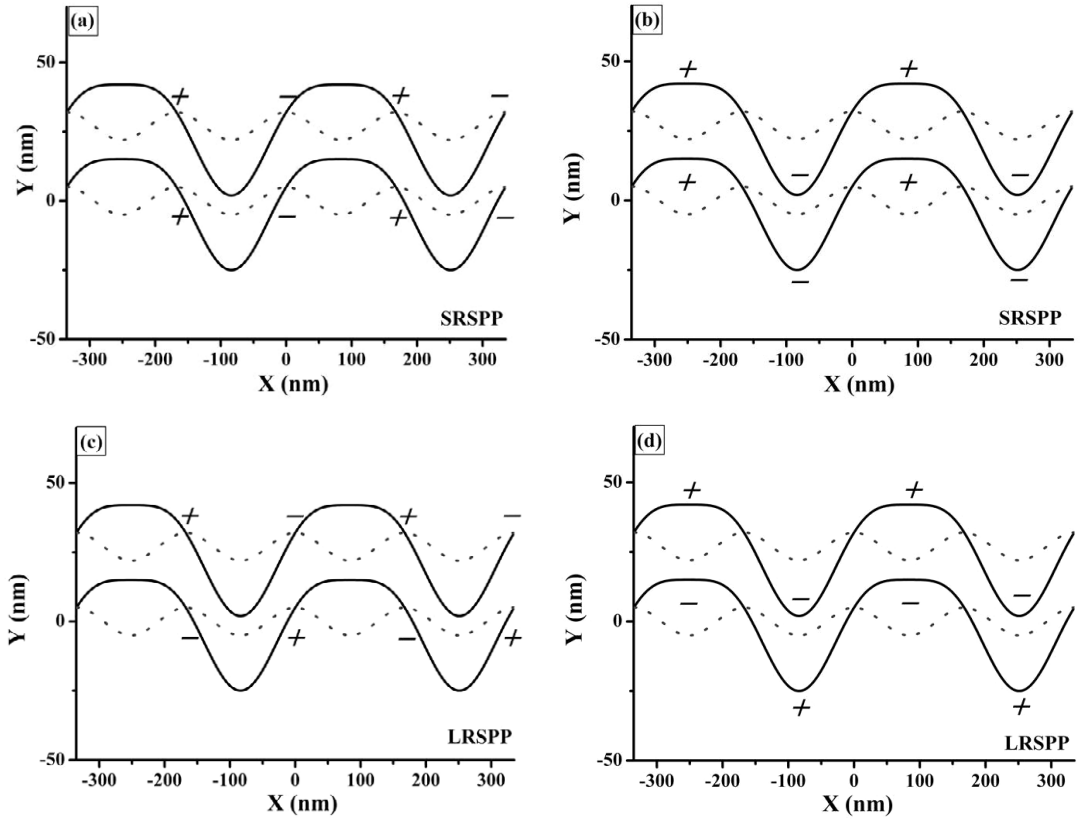

Figure 6. Schematics showing the positions of maximum surface charge density of the possible standing wave coupled modes for normal incidence that may be excited on the structure. The black lines represent the thin metal grating. The dashed lines indicate the $2k_g$ component of the grating.

and two SRSPP modes respectively. Figure 6 schematically shows the positions of maximum surface charge density of these four possible solutions relative to the $2k_g$ component of the grating (indicated as dashed lines). For one possible solution of the lower frequency self-crossing point (the SRSPP self-crossing point), as shown in figure 6(a), the positions of maximum surface charge density occur at the peaks of the $2k_g$ component (low energy, ω^-), while equivalent positions on the bottom surface occur at the troughs of the $2k_g$ component (high energy, ω^+). Figure 6(b) shows that another possible solution with the correct symmetry is that on the top interface the surface charge density maxima occur at the troughs of the $2k_g$ component (high energy, ω^+) and the surface charge density maxima occur at the peaks of the $2k_g$ component (low energy, ω^-). From this it is apparent that the two possible solutions for SRSPP modes will have the same energy. Hence, at the SRSPP self-crossing point, even with the existence of a $2k_g$ component in the profile, we should expect that *no* band gap arises. For the same reason, as shown in figures 6(c) and (d), the two possible solutions for the LRSPP modes will also have the same energy. This explanation can also be used to explain the lack of band gap at the LRSPP self-crossing point. Figure 7 shows the H_z profiles together with the instantaneous E_{xy} vector fields for the SRSPP ($f = 0.475 \times 10^{15}$ Hz) and the LRSPP ($f = 0.581 \times 10^{15}$ Hz) excited at normal incidence on the structure as described for figure 4(b) (incident from second prism with $\phi = -\pi/2$). The same discussions and arguments as given for figure 5 can be applied to the case of figure 7.

Now we have seen that even with the existence of a $2k_g$ component in the profile of a conformal thin silver grating there are *no* band gaps at normal incidence for both the SRSPP and the LRSPP modes. It is worth investigating how to open up the band gaps at normal incidence for thin silver gratings. Figure 8 shows the model band structure of a thin silver grating with non-identical corrugations on each of interfaces; the modes are indicated by white dashed lines. The profile describing the structure is given by $[20\sin(k_g x) + 5\sin(2k_g x - \pi/2)]$ nm for the bottom surface and $[20\sin(k_g x) + 5\sin(2k_g x \pi/2) + 27]$ nm for the top surface. Note that the phase shifts ϕ on the top and bottom surfaces are $-\pi/2$ and $+\pi/2$ respectively. Obviously in figure 8 two band gaps open up at normal incidence for the SRSPP and the LRSPP modes respectively.

Again by investigating the positions of maximum surface charge density of possible solutions relative to the $2k_g$ component of the grating we can explain why the band gaps open up for the SRSPP and the LRSPP modes at normal incidence for non-conformal thin silver gratings. Figure 9 schematically shows the surface charge density maxima positions of two possible SRSPP solutions. For one possible solution, as shown in figure 9(a), the positions of maximum surface charge density occur at the peaks of the $2k_g$ component (low energy, ω^-), and equivalent positions on the bottom surface also occur at the peaks of the $2k_g$ component

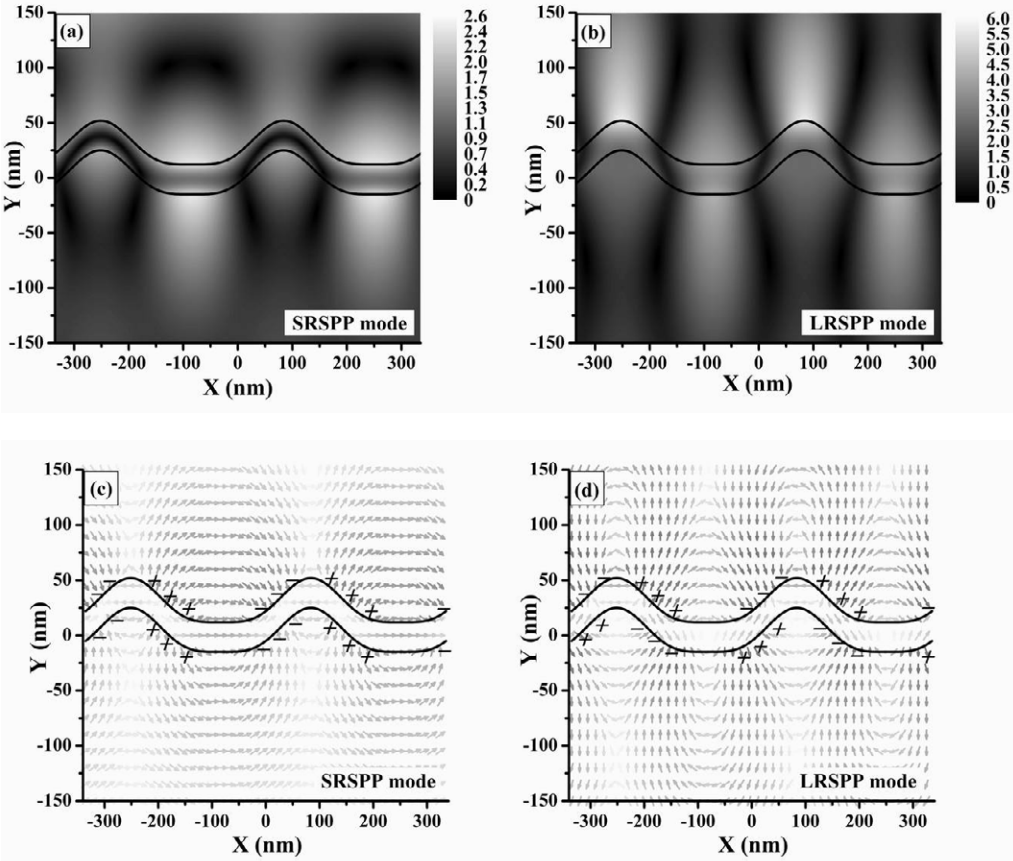

Figure 7. Time averaged H_z component of the fields of (a) the SRSPP and (b) the LRSPP modes that can be excited at normal incidence, together with the instantaneous E_{xy} vector fields for (c) the SRSPP and (d) the LRSPP modes on the same structure as described in figure 4(b) (incident from the second prism with $\phi = -\pi/2$). The continuous black lines represent the thin metal grating.

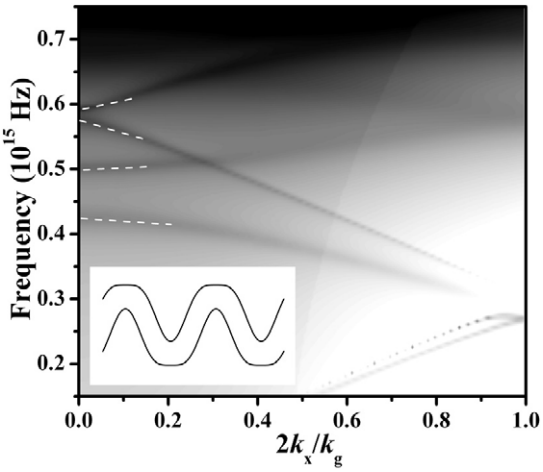

Figure 8. The model band structures for a thin silver grating having profiles $[20\sin(k_g x) + 5\sin(2k_g x - \pi/2)]$ nm for the bottom surface and $[20\sin(k_g x) + 5\sin(2k_g x + \pi/2) + 27]$ nm for the top surface at an azimuth angle of $\varphi = 0°$. The inset graph corresponds to the grating that has been used in the calculations.

(low energy, ω^-). Similarly, for another possible solution, as shown in figure 9(b), the surface charge density maxima occur at the troughs of the $2k_g$ component (high energy, ω^+) on both the top and bottom interfaces. Thus the two possible solutions for SRSPP modes will have different energies, ω^- for low energy branch and ω^+ for the high energy branch, and a band gap arises at the SRSPP self-crossing point. For similar reasons, at the LRSPP self-crossing point a band gap will also open up.

If we examine the thin silver grating shown in figure 8 carefully, one can see that the width of the vertical cross section of the grating is modulated in the x-direction. This leads to the question is this thickness modulation the only required condition to open up the band gaps at normal incidence for the SRSPP and the LRSPP modes. Figure 10 shows the model band structure of a non-conformal thin silver grating, in which the SRSPP and the LRSPP modes scattering from $\pm k_g$ are indicated by white dashed lines. The profile describing this structure, as shown in the inset graph of figure 10, is given by $[10\sin(k_g x)]$ nm for the bottom surface and $[-10\sin(k_g x) + 27]$ nm for the top surface. Obviously in such a thin grating which has no $2k_g$ component the thickness of the silver film is also modulated in the x-direction. However, as shown in figure 10, *no* such band gaps are opened up at normal incidence for SRSPP and LRSPP modes. This implies that two conditions, non-identical corrugations on each side of the thin grating and the existence of a $2k_g$ component, must be fulfilled to open up band gaps at normal incidence for the SRSPP and LRSPP modes.

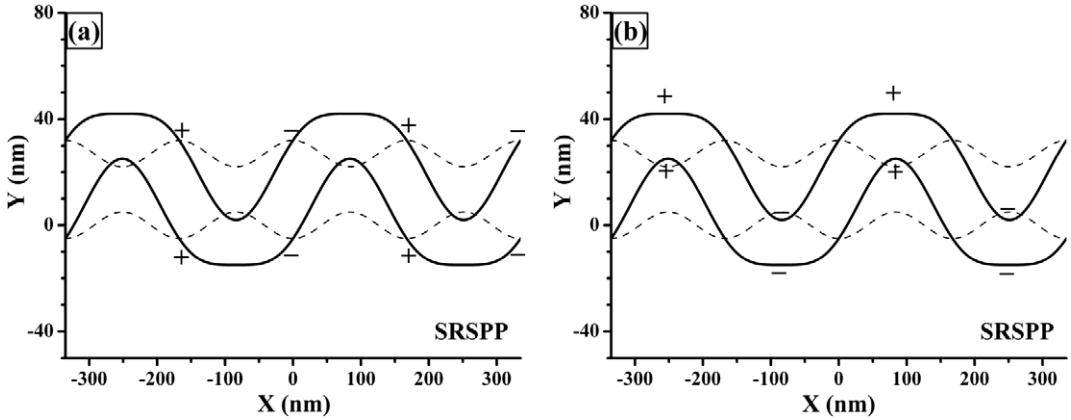

Figure 9. Schematics showing the positions of maximum surface charge density of the possible short range SPP modes for normal incidence that may be excited on the structure. The black lines represent the thin metal grating. The dashed lines indicate the $2k_g$ component of the grating.

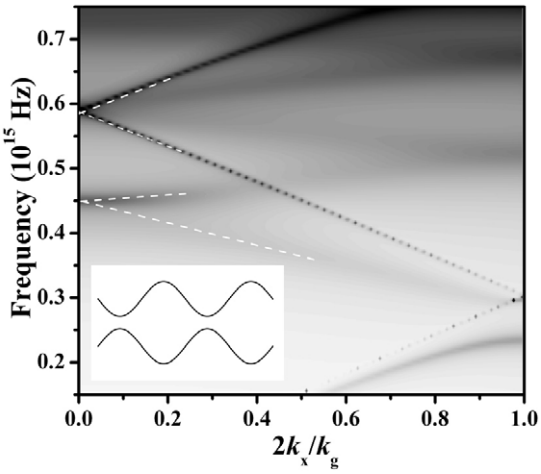

Figure 10. The model band structure for a non-conformal thin silver grating having the profiles $[10\sin(k_g x)]$ nm for the bottom surface and $[-10\sin(k_g x) + 27]$ nm for the top surface at an azimuth angle of $\varphi = 0°$. The inset graph corresponds to the grating that has been used in the calculations.

3. Summary

In this study the two coupled surface plasmon polaritons (the SRSPP and the LRSPP) on a thin symmetrically surrounded silver film (27 nm thick) have been investigated experimentally and modelled theoretically in the visible range. Wavelength-dependent absolute reflectivity data for TM polarized incident radiation at different polar angles in the 'classical' mount leads to a mapping of the dispersion curve of the various SPP modes as a function of frequency and in-plane wavevector. It is shown that the $2k_g$ component in the grating profile is the key factor leading to the appearance of band gaps in these relatively shallow gratings. Interestingly, the band gap which would appear on a single metal surface (supporting just the SPP mode) for normal incidence radiation does not appear in the two self-crossing points of the LRSPP modes and the SRSPP modes at normal incidence. This is because of the symmetry of the standing wave states of the expected two modes relative to the $2k_g$ component of the grating. However, a band gap does appear within the Brillouin zone, formed by the anti-crossing of the LRSPP scattered by $+k_g$ and the SRSPP scattered by $-k_g$. Finally we considered the case where the two corrugations on each surfaces are not conformal, and we focused on the self-crossing points at $k_x = 0$ (normal incidence). We found that only when two conditions that the structure is non-conformal and has a $2k_g$ component are fulfilled, so the band gaps open at $k_x = 0$ for both the LRSPP and the SRSPP modes.

Acknowledgments

Z Chen acknowledges the financial support of an Overseas Research Studentship and the University of Exeter.

References

[1] Raether H 1988 *Surface Plasmons on Smooth and Rough Gratings* (Berlin: Springer)
[2] Otto A 1968 *Z. Phys.* **216** 398
[3] Kretschmann E and Raether H 1968 *Z. Naturf.* a **23** 2135
[4] Wood R W 1902 *Phil. Mag.* **4** 396
[5] Ritchie R H, Arakawa E T, Cowan J J and Hamm R N 1968 *Phys. Rev. Lett.* **21** 1530
[6] Sobnack M B, Tan W C, Wanstall N P, Preist T W and Sambles J R 1998 *Phys. Rev. Lett.* **80** 5667
[7] Schoenwald J, Burstein E and Elson J M 1973 *Solid State Commun.* **12** 185
[8] Boersch H, Geiger J, Imbusch A and Niedrig N 1966 *Phys. Lett.* **22** 146
[9] Otto A 1969 *Z. Phys.* **219** 227
[10] Sarid D 1981 *Phys. Rev. Lett.* **47** 1927
[11] Stegeman G I, Burke J J and Hall D G 1982 *Appl. Phys. Lett.* **41** 906
[12] Hickernell R K and Sarid D 1986 *J. Opt. Soc. Am.* B **3** 1059
[13] Inagaki T, Motosuga M, Arakawa E T and Goudonnet J P 1985 *Phys. Rev.* B **32** 6238
[14] Dutta Gupta S, Varada G V and Agarwal G S 1987 *Phys. Rev.* B **36** 6331
[15] Ebbesen T W, Lezec H J, Ghaemi H F, Thio T and Wolff P A 1998 *Nature* **391** 667

[16] Ghaemi H F, Thio T, Grupp D E, Ebbesen T W and Lezec H J 1998 *Phys. Rev.* B **58** 6779
[17] Kim T J, Thio T, Ebbesen T W, Grupp D E and Lezec H J 1999 *Opt. Lett.* **24** 256
[18] Hooper I R and Sambles J R 2004 *Phys. Rev.* B **70** 045421
[19] Chandezon J, Dupuis M T, Cornet G and Maystre D 1982 *J. Opt. Soc. Am.* **72** 839
[20] Bryan-Brown G P, Jory M C, Elston S J and Sambles J R 1993 *J. Mod. Opt.* **40** 959
[21] Wood E L, Sambles J R, Cotter N P K and Kitson S C 1995 *J. Mod. Opt.* **42** 1343
[22] Watts R A, Preist T W and Sambles J R 1997 *Phys. Rev. Lett.* **79** 3978
[23] Palik E D (ed) 1985 *Handbook of Optical Constants of Solids* (New York: Academic)
[24] Barnes W L, Preist T W, Kitson S C and Sambles J R 1996 *Phys. Rev.* B **54** 6227